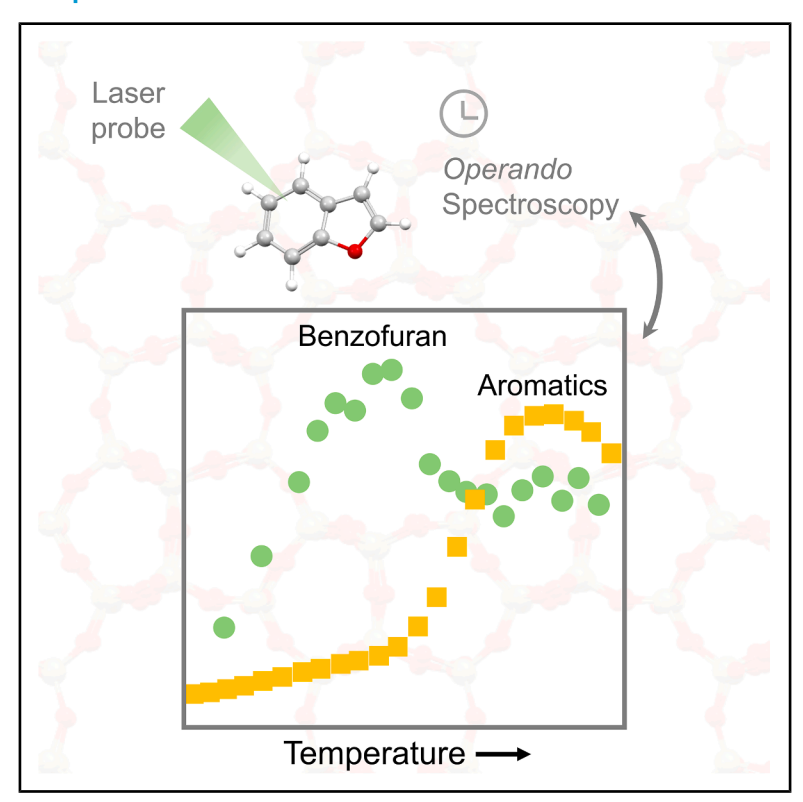
Unraveling the effect of zeolite topology on the mechanism of furan deoxygenation to aromatics using *operando* Raman spectroscopy

Graphical abstract



Authors

Emma Campbell, James Mattock, Monik Panchal, ..., Michael Towrie, Ines Lezcano-Gonzalez, Andrew M. Beale

Correspondence

ines.lezcanogonzalez@manchester.ac.uk (I.L.-G.), andrew.beale@ucl.ac.uk (A.M.B.)

In brief

Operando Kerr-gated Raman spectroscopy, combined with UV-vis spectroscopy and theoretical calculations, reveals how zeolite topology shapes catalytic fast pyrolysis chemistry, highlighting the unique role of benzofuran intermediates.

Highlights

- Zeolite framework topology governs the chemical pathways of the CFP reaction
- Benzofuran dominates ZSM-5 chemistry, directing monocyclic aromatics selectivity
- Benzofuran is not a coke precursor in CFP chemistry
- ZSM-5 provides sufficient spatial constraint to prevent rapid hydrocarbon conjugation







Article

Unraveling the effect of zeolite topology on the mechanism of furan deoxygenation to aromatics using *operando* Raman spectroscopy

Emma Campbell,^{1,2,3} James Mattock,⁴ Monik Panchal,^{2,5} Peixi Cong,^{2,6} Stefan Kucharski,² Christopher S. Blackman,² Michael J. Watson,⁷ Paul Cox,⁴ Igor V. Sazanovich,⁸ Michael Towrie,⁸ Ines Lezcano-Gonzalez,^{2,3,9,10,*} and Andrew M. Beale^{2,3,11,*}

SUMMARY

Catalytic fast pyrolysis (CFP) of biomass has the potential to be a drop-in solution for chemicals and fuels beyond oil. However, understanding the relationship between catalyst structure and function remains a critical challenge hindered by the fast reaction dynamics. Here, we report an *operando* Kerr-gated Raman study, a powerful yet underexplored technique in catalysis research that allows for real-time monitoring of the different stages of the CFP reaction. In combination with UV-visible (UV-vis) spectroscopy and theoretical calculations, we demonstrate how the zeolite topology governs the chemical pathways and final product selectivity, influencing the type and fate of adsorbed intermediates. In addition to observing early formation of monomeric and dimeric furan, we demonstrate that benzofuran dominates the chemistry of the reaction on ZSM-5, playing a key role in the selective formation of monocyclic aromatic hydrocarbons. Furthermore, a pathway that deems benzofuran directly responsible for generating polyaromatic hydrocarbons is ruled out.

INTRODUCTION

Global use of biomass is expected to intensify in the coming decades, and as the pressure to implement sustainable solutions increases, there is an urgent need for more efficient processes for its chemical transformation. Catalytic fast pyrolysis (CFP) is a process that can be used to convert lignocellulosic biomass to high-value products such as olefins, oxygenates, and substituted aromatics; i.e., the "drop-in" platform chemicals and/or fuels of the future. ¹⁻³ Non-catalytic pyrolysis of biomass typically results in bio-oils with high oxygen content, leaving them acidic, unstable, and miscible with water. Dehydration, decarboxylation, and decarbonylation of the pyrolysis vapors take place during CFP to give oils with more favorable properties. ¹⁻³

Zeolites can be used as catalysts for CFP, and zeolite topology and properties lead to drastic differences in product distribution and lifetime. ^{4,5} For example, ZSM-5, as a 3-dimensional,

medium-pore zeolite, consistently gives the highest aromatic yield, while 3-dimensional structures with larger pores, such as zeolite Y and zeolite beta, give high selectivity to monocyclic aromatics but overall low yields due to rapid coke deposition. Small-pore zeolites, in contrast, produce more oxygenated species with little to no aromatic species formed.⁴ To finetune product selectivity and suppress coke formation, the acidity of ZSM-5 has been modulated by incorporating metal species such as Ga or ZrO₂.⁶⁻⁸ Additionally, co-feeding strategies (e.g., with methanol) have been employed to further influence reaction pathways and product distribution.^{9,10}

Overall, ZSM-5 shows both superior selectivity to high-value products and superior lifetime, ⁴ although the specific mechanistic aspects governing its exceptional performance are still not fully understood. Some research points toward an independence of the reaction on the biomass feed, and so CFP is often discussed as a hydrocarbon pool (HCP) mechanism akin to the methanol-to-hydrocarbons (MTH) reaction, where a group of



¹School of Chemistry, Cardiff University, Cardiff University Main Building, Park Place, Cardiff CF10 3AT, UK

²Department of Chemistry, University College London, 20 Gordon Street, London WC1H 0AJ, UK

³UK Catalysis Hub, Research Complex at Harwell, Rutherford Appleton Laboratory, Harwell, Oxford OX11 0FA, UK

⁴School of Pharmacy and Biomedical Sciences, University of Portsmouth, St Michael's Building, White Swan Road, Portsmouth PO1 2DT, UK

⁵Department of Chemistry, Durham University, Lower Mount Joy, South Road, Durham DH1 3LE, UK

⁶Department of Materials, University of Oxford, Parks Road, Oxford OX1 3PH, UK

⁷Johnson Matthey, Johnson Matthey Technology Centre, PO Box 1, Belasis Avenue, Billingham TS23 1LB, UK

⁸Central Laser Facility, Research Complex at Harwell, Rutherford Appleton Laboratories, Harwell Campus, Didcot OX11 0QX, UK

⁹Department of Chemical Engineering, School of Engineering, University of Manchester, Oxford Road, Manchester M13 9PL, UK

¹⁰University of Manchester at Harwell, Diamond Light Source, Harwell Science and Innovation Campus, Didcot, Oxfordshire OX11 0DE, UK
¹¹Lead contact

^{*}Correspondence: ines.lezcanogonzalez@manchester.ac.uk (I.L.-G.), andrew.beale@ucl.ac.uk (A.M.B.) https://doi.org/10.1016/j.xcrp.2025.102858





catalytically active hydrocarbons is required to build up in the zeolite pores^{11,12} before fresh reactants (biomass vapors) can be deoxygenated.^{13,14} Evidence of this type of reaction is provided indirectly by the induction period required before effective deoxygenation takes place¹⁴ and by ¹³C/¹²C isotopic exchange experiments, ¹³ and certainly the reaction seems to be more complicated than direct depolymerization.¹³

For a direct inspection of the mechanism, operando and in situ methods offer the possibility of directly observing intermediates and identifying their relationship with catalytic performance. Nevertheless, while most CFP contributions focus on synthesis and reactivity, precise characterization studies, particularly under reaction conditions, are scarce. 15-18 Conventional optical techniques, such as Fourier transform infrared (FTIR) and UVvisible (UV-vis) spectroscopy, are limited by optical attenuation due to sample darkening by carbon buildup. Raman spectroscopy is a particularly advantageous technique for characterizing carbonaceous species and intermediates, such as those involved in the CFP reaction, but is often hindered by strong emission arising from laser excitation of the sample. 19 In this study, we combined operando Kerr-gated Raman spectroscopy with theoretical simulations to rationalize the reported different activity of 4 active zeolites in CFP,4 enabling us to correlate the spectroscopic signatures from characteristic reaction intermediates with deviations in catalytic performance. Kerr-gated Raman spectroscopy allows discrimination between Raman scattering and fluorescence based on the temporal differences of the two processes after short-pulse optical excitation. By using short (3 ps) laser pulses and a fast optical gate, we were able to filter out interfering fluorescence from the zeolite samples.^{20,21} Additionally, the application of operando UV-vis spectroscopy helps to rationalize the extent of hydrocarbon conjugation on the zeolites until sample darkening becomes too severe during the reaction for the reasonable detection of signals. Overall, these combined methods have been very successful previously in deciphering HCP chemistry in MTH.²

Given the complexity of biomass composition, appropriate model compounds are required for mechanistic studies. Several research works point to the importance of furan as an intermediate in non-catalytic pyrolysis from either glucose⁵ or levoglucosan as a main product of lignocellulose pyrolysis²² and is therefore commonly used as a model for studying biomass upgrading.^{2,3,23,24} In addition, furan has an appropriate effective hydrogen/carbon ratio for modeling biomass (H/C_{eff} = 0.5) and is thermally stable. Here, we report spectroscopy results of CFP of furan on the zeolites ZSM-5, ferrierite, zeolite Y, and zeolite beta, all in proton form (see Tables S1 and S2 and Figure S1 for characterization details).

RESULTS AND DISCUSSION

Impact of channel size and dimensionality on furan oligomerization

Oligomerization of furan at room temperature on ZSM-5, zeolite Y, zeolite beta, and ferrierite catalyst materials was first examined to understand the influence of both channel size and dimensionality on the early CFP intermediates, originating from initial furan adsorption on the zeolite Brønsted acid sites.

The introduction of furan (a clear yellow liquid) at room temperature on zeolites caused the material to immediately turn a red or orange color (Figure S2) as furan oligomerizes on the zeolite acid sites to different degrees. This has been observed by Spoto et al., who studied the oligomerization of 5-membered heterocycles on zeolites by UV-vis and FTIR spectroscopy, 25 and Cheng and Huber via temperature-programmed reaction (TPR) combined with thermogravimetric analysis (TGA). Nevertheless, the reported data were not enough to precisely elucidate the type of structure present. 14

Here, UV-vis spectroscopy was initially used to investigate the extent of conjugation (i.e., of furan polymerization) and charged state of the hydrocarbon (Figure S3). Comparison between the experimental and calculated UV-vis spectra for protonated furan and oligomers of 2 or 3 furan molecules suggests that we observe a mixture of all 3 types of species, although the broad and convoluted bands prevent drawing definitive conclusions. For the medium-pore zeolites, ZSM-5 and ferrierite, this is illustrated by distinct absorbance bands with maxima at 222, 280, 410, and 540 nm. For the large-pore zeolites, zeolite Y and zeolite beta, the bands are more convoluted. In zeolite Y, the strong absorbance extends toward the near-infrared region, indicating that, in the large internal volumes of this zeolite (micropore volume given in Table S1), furan polymerizes to a more extended structure than the 3-ring oligomers.

More precise assignments can be obtained by the combination of Kerr-gated Raman spectroscopy and theoretical calculations. Figure 1A displays the experimental Kerr-gated Raman spectra after furan adsorption on the zeolites, and the calculated Raman spectra for the proposed dimer and trimer, as well as protonated furan, are given in Figure 1B. The spectra can be generally broken down into 4 regions of interest, as highlighted in the figures, with C=C stretching vibrations at 1,580-1,630 cm⁻¹ (gray highlight) and mixtures of vibrations at approximately 1,500-1,530 (blue), 1,360-1,390 (pink), and 1,160-1,210 cm⁻¹ (yellow). In agreement with the UV-vis spectroscopy results, the Kerr-gated Raman spectroscopy data show the formation of protonated furan and oligomeric species, seen by the comparison of experimental signals against the simulated spectra,- with the degree of conjugation being dependent on the zeolite structure.

Medium-pore zeolites show the highest frequency of C=C stretch, in line with the calculated spectrum of the protonated dimer, while the large-pore zeolite Y displays a redshift in the C=C stretch (at 30 cm⁻¹ lower), consistent with the 3-ring oligomer. Two overlapping bands, in contrast, can be observed in this region for zeolite beta, at 1,580 and 1,620 cm⁻¹, attributed to a mixture of oligomers with 2 and 3 furan molecules. The prevalence of 3-ring oligomers on the larger-pore zeolites is further confirmed by the presence of an additional band in the 1,500- to 1,530-cm⁻¹ region, alongside the stronger vibrations at 1,380 cm⁻¹, corresponding to the trimer as per the calculated spectra. Accordingly, the Kerr-gated Raman spectroscopy results indicate that the protonated dimer dominates in ferrierite and ZSM-5, while zeolite beta displays the clearest mixture of both species, and zeolite Y is dominated by the larger structure, enabling a more precise characterization of the species present.

Article



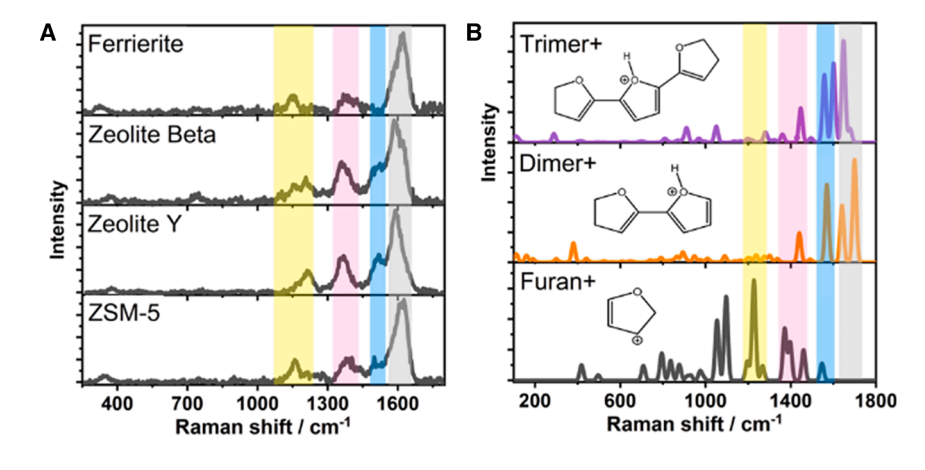


Figure 1. Impact of channel size and dimensionality on furan oligomerization

Kerr-gated Raman spectra were collected after the adsorption of furan on 4 zeolites (ZSM-5, ferrierite, zeolite Y, and zeolite beta) (A) and the simulated Raman spectra of furan and a dimer and trimer of furan (B). Measurements were performed at room temperature. Excitation wavelength was 400 nm.

benzofuran was not detected as a product here by MS, which we propose to be due to the strong adsorption of this molecule on the zeolite Brønsted acid sites, possibly protonated at the O atom, in line with the theoretical data

shown in Figure 3B. Formation of this species from furan and furan oligomers is further evidenced by the *operando* UV-vis data (Figure S5), which show a gradual attenuation in absorbance at 290 and 415 nm in this temperature range.

With increasing reaction temperatures, above 325°C, the relative intensity of the benzofuran vibration at 1,540 cm⁻¹ is seen to steadily decrease (Figures 2B and 3A), whereas a gradual climb in intensity is detected for the *m/z* values for both benzene and branched aromatics (m/z 78 and 91, respectively), indicating a correlation between the consumption of surface-adsorbed benzofuran and the formation of aromatic products. While this has been a long-debated topic, and many assumptions and speculations can be found in the literature data, such a correlation provides unambiguous evidence of the formation of aromatics from benzofuran and, therefore, of the role of these surface-adsorbed species as crucial intermediates for the CFP reaction, directing final product selectivity. Besides aromatics, water and carbon monoxide are also detected by MS at this stage of reaction, suggestive of benzofuran intermediates being hydrolyzed to aromatic products, with oxygen removed as carbon monoxide (decarbonylated) or potentially as water dehydrated to a branched aromatic such as ethylbenzene.

Above 375°C, the band at 1,540 cm⁻¹ becomes indistinguishable (Figure 2B), and a broad signal with a maximum at 1,605–1,625 cm⁻¹ develops, attributed to the C=C stretching of trapped monocyclic aromatic species that have been unable to diffuse out of the zeolite as a product. Some bands at 1,000–1,500 cm⁻¹ are too weak to be resolved from the spectral noise. These are probably due to an array of different signals and species, where the bonds are not affected by any resonance enhancement effect, including a mixture of signals corresponding to CH₂ deformations, CC stretches, and CH twists.³³

A further temperature increase to 500°C and above (Figure 2C) sees a decline in the formation of aromatic products (by MS), while the generation of bi- and polycyclic aromatic hydrocarbons is observed by the development of a strong Raman band at 1,380 cm⁻¹, corresponding to ring-breathing modes, ^{19,21,34} alongside a shoulder at 1,440 cm⁻¹, attributed to polyaromatic hydrocarbons with bent structures, such as 9H-fluorene or phenanthrene. ^{19,34}

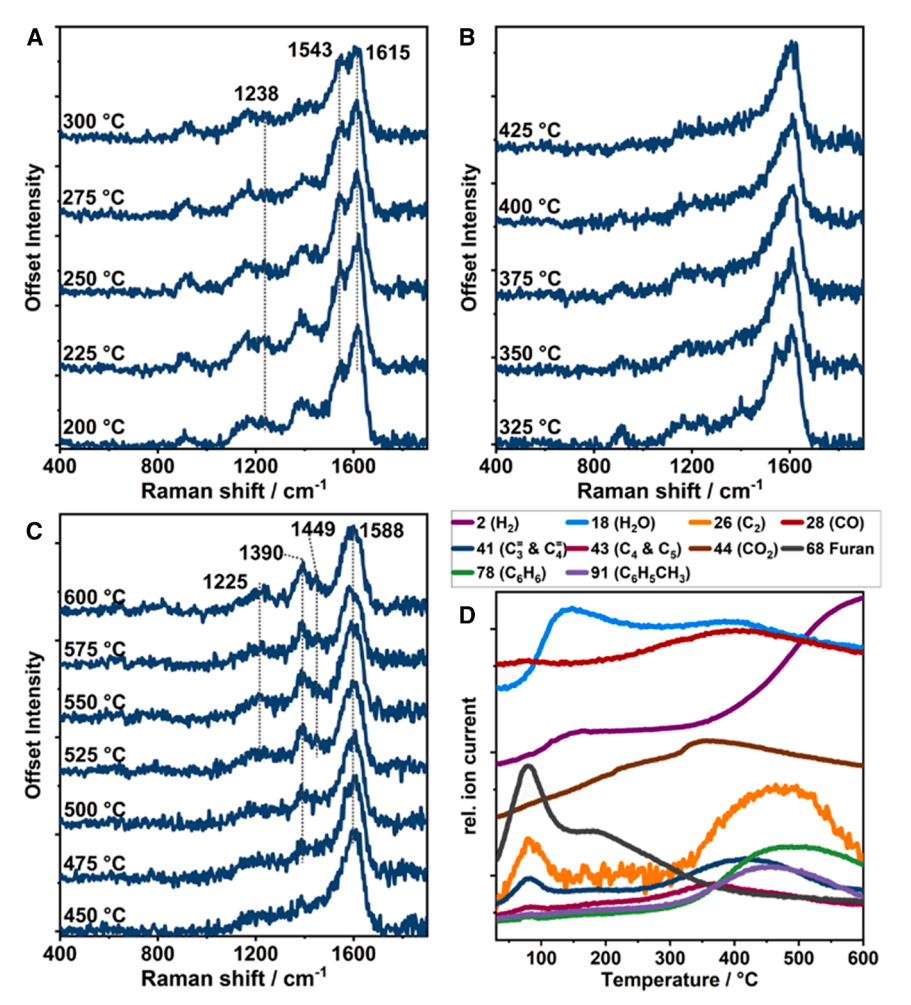
Mechanistic insights into aromatics formation on ZSM-5

The reaction steps and intermediates for aromatic formation during CFP was assessed by operando Kerr-gated Raman spectroscopy. Due to rapid deactivation of the catalyst, we adopted a method used by several groups, TPR, whereby the catalyst is saturated with the reactant and then subjected to a linear temperature increase (up to 600°C at a rate of 5°C min⁻¹) under an inert gas flow. ^{23,26-28} While this approach was used in previous works to disentangle the effect of the reaction temperature on product distribution, when combined by operando spectroscopic methods like in our work, it allows correlations between adsorbed intermediates and evolved reaction products, enabling at the same time, to follow the reaction in time and temperature-dependent steps without the concern for rapid deactivation. The following observations are generally made in experiments with all four zeolites. At 50°C-160°C (low T), the formation of primary products is observed as water and carbon dioxide by mass spectrometry (MS), and above 400°C (high T), secondary products are detected in the outlet gas stream, typically aromatic and olefinic hydrocarbons.

In ZSM-5, first an initial desorption of furan is detected by MS below 100°C, followed by the detection of water from the reactor between 120°C and 200°C. Changes in Raman spectra collected in this temperature range show a general broadening of signals and the development of a strong Raman band at 1,540 cm⁻¹. Such a strong vibration (marked in Figure 2A), which gradually increases up to 300°C (Figures 2A and 3A), can be assigned to the C=C stretch in the 5-membered ring of benzofuran and is accompanied by a weaker signal at 1,225 cm⁻¹ due to the CO stretch and a strong band at 1,615 cm⁻¹, attributed to the C=C stretch in the 6-membered ring, providing a direct spectroscopic fingerprint for the formation of this intermediate.²⁹ Calculations to simulate Raman spectra of a benzofuran intermediate show a likely intermediate as a cationic benzofuran molecule that is protonated in the oxygen atom (Figure 3B), where a very strong signal is calculated in the C=C stretching region of the charged molecule, which might explain why this signal is so strong in our experimental data.

Benzofuran is discussed in the literature to form from the Diels-Alder condensation of two furan molecules, ^{30–32} which explains the water detected in this period by MS (Figure 2D). However,





Data from a parallel UV-vis experiment is shown in Figure S5 and indicate increasing conjugation with temperature. Absorbance increases across the spectra and more so at higher wavelengths at 550 and 650 nm, as conjugated species tend toward more extended coking agents, possibly such as small, graphitelike polyaromatics.35 We note very high values of Kubelka-Munk absorbance beyond 10 that correspond to percent reflectance of <5%, where not only values of Kubelka-Munk (K-M) absorbance are strongly exaggerated, but it is also quite possible that the spectra are prone to artifacts, which can be quite common when using diffuse reflectance techniques in strongly absorbing samples.^{36,37} These results clearly illustrate the limitation of conventional optical techniques for the study of the CFP reaction under in situ and operando conditions, demonstrating in particular that Kerr-gated Raman spectroscopy, with spectral assignments supported by high-end computational chemistry methods, provides a significantly more reliable technique to investigate the intricate chemistry of this complex reaction.

Role of framework topology in catalytic intermediates

To further assess the relevance of surface-adsorbed benzofuran as well as the effect of the zeolite topology on the mechanistic pathway, analogous experiments were performed on zeolite Y,

Figure 2. Mechanistic insights into aromatic formation on ZSM-5

Kerr-gated Raman data were collected during the TPR of furan on H-ZSM-5 between (A) 200°C and 300°C, (B) 325°C and 425°C, and (C) 450°C and 600°C and (D) MS data collected simultaneously in the same experiment during the temperature ramp. Measurements were performed at increasing reaction temperatures (up to 600°C at a rate of 5°C min⁻¹) under He gas flow after furan saturation at room temperature. Excitation wavelength was 400 nm. We note that experiments repeated with a UV laser (267 nm) failed to capture all intermediates due to strong emission (Figure S4).

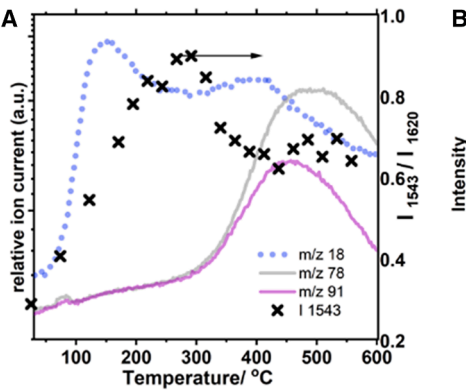
zeolite beta, and ferrierite. Zeolite Y and beta are 3-dimensional zeolites with larger pore sizes (12-membered ring pore openings) compared to ZSM-5. While zeolite Y features large, interconnected cages, the narrower channels in beta can influence shape-selective catalysis. Ferrierite, in contrast, although formally 2-dimensional with both 10-ring and 8-ring channels, behaves as a 1-dimensional system, as furan (kinetic diameter ~5.1 Å) cannot diffuse through the smaller channels.

In contrast to the experiment in ZSM-5, the reaction on ferrierite is notably different according to all of Kerr-gated Raman and UV-vis spectroscopy and MS data. In the MS results shown in Figure 4A, during the first 200°C of ramp-

ing temperature, only desorption of a small amount of furan is recorded, and later dehydration takes place at higher temperatures above 200°C. Almost immediately after the release of water, some propene and carbon dioxide are formed, as observed by *m/z* 41 and 44, respectively. No aromatic products are, however, detected from the reaction, in line with the work of Jae et al., who showed a similar result for biomass pyrolysis on this zeolite catalyst.⁴

Kerr-gated Raman spectra (illustrated in Figure 4B) show a decreasing C=C stretch frequency. The overall decrease from 1,621 to 1,600 cm⁻¹ between 30°C and 300°C indicates the loss of the dimer structures, which, according to our calculations, give the highest frequency C=C stretch vibration. By Raman spectroscopy, the remainder of the signals are too weak to be properly resolved. Consumption of 2-ring furan oligomers is also detected by UV-visible spectroscopy (Figure S6), showing a clear loss of the absorbance band at 415 nm, along with the weakening of the band of protonated furan at 290 nm. Interestingly, consumption of furan and 2-ring furan oligomers is accompanied by the detection of water above 200°C, as seen by MS (*m*/*z* 18; Figure 4A), where the high temperature would suggest this to be due to a condensation reaction, ruling out water from only desorption from the zeolite, although the





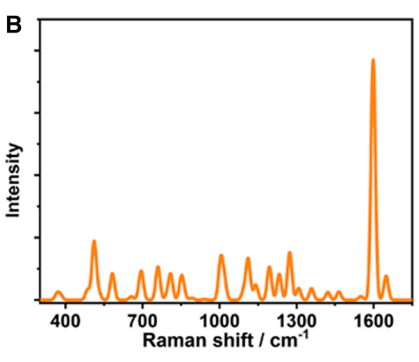


Figure 3. Identification and evolution of benzofuran intermediates

(A) Shown is a plot of ratio of I_{1,543} to I_{1,615} (as the most intense band in the spectrum) with increasing temperature, overlaid by *m/z* traces 18, 78, and 91 as collected by MS for water (blue dot), benzene (gray line), and branched aromatics (purple line), from data collected during TPR of furan on H-ZSM-5 and (B) calculations of Raman of free, gas-phase O-protonated benzofuran molecules.

characteristic vibrations of adsorbed benzofuran are not observed in the Raman spectra. Huber and colleagues showed that water in the presence of furan can cause direct decarboxylation to give carbon dioxide and propene.³⁸ The direct decarboxylation of furan and furan dimers would appear to be a significant process in the ferrierite system, given the coincidence in temperature of the carbon dioxide and propene detected by MS (Figure 4A).

As the temperature is further increased to 400°C, some ethane or ethene is detected by MS (*m*/*z* 26), which ceases above 525°C. By Raman spectroscopy, the species remaining on the surface likely encompass amorphous carbon at this stage and are better characterized in the quenched spectrum at the end of the experiment, as shown in Figure 6B and discussed later.

When studying zeolite Y (Figure 5A), during the initial temperature increase below 100° C, desorption of furan is more significant, in line with the higher overall surface area of this material (data given in Table S1) available for furan physisorption. Also, water is released at a lower temperature than in the other materials, suggesting that condensation reactions are taking place earlier. At intermediate temperatures, a strong contribution to the MS data from m/z 43 indicates formation of paraffins that was not observed in either reaction of the medium-pore zeolites. As in ZSM-5, aromatic products are detected at higher temperatures by MS, from 350° C.

By Raman, with increasing temperatures, a broadening of signals is observed around the C=C stretching vibration centered at 1,590 cm⁻¹, and a strong signal at 1,532 cm⁻¹ that was formed upon initial furan adsorption (as shown in Figure 1A) remains constant. Interestingly, with increasing temperature to 300°C, growth or broadening in the region from 1,550 up to 1,600 cm⁻¹ is observed (Figure 5E), corresponding to C=C stretches in a plethora of potential species from monocyclic aromatic hydrocarbons (at 1,600 cm⁻¹) to conjugated olefinic species of varying chain lengths (1,550-1,580 cm⁻¹). 19,21,33 These changes correlate with the release of paraffins that interact weakly with Brønsted acid sites of the zeolite and therefore diffuse out of the reactor as products, while conjugated olefins or aromatics remain strongly attracted with the potential for further reactivity. For the formation of paraffins in this reaction, as in other hydrocarbon conversion reactions, hydride transfer mechanisms are required intermolecularly, 39 an example of which is highlighted in Figure 5C. While zeolite Y displays slightly weaker Brønsted acid strength

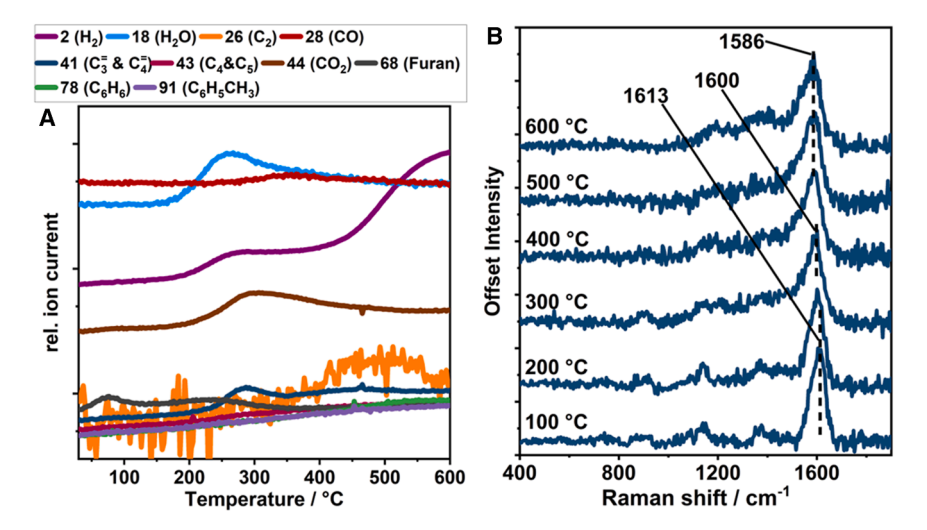
than the other zeolites examined, the product distribution reveals a strong propensity for bi-molecular coupling reactions. This is primarily attributed to its large pore size and open cage structure, which facilitate the diffusion and interaction of adsorbed molecules. These topological features promote hydrogen transfer reactions and contribute to the higher paraffin-to-olefin ratio observed, highlighting that pore architecture plays a more decisive role than acidity in directing product selectivity in this case. At high temperatures above 400°C, two broad and flat bands develop, centered at 1,100 and 1,500 cm⁻¹, and the overall spectrum, particularly the presence of D and G bands, suggests the presence of non-aromatic type carbonaceous species. Data and discussion of the corresponding UV-vis experiment are given in Figure S7.

During the reaction on zeolite beta, after desorption of physisorbed furan and water release from condensation reactions, as observed by MS (Figure 5D), again we observe a paraffinic product by a response at m/z 43 at intermediate temperatures with maximum production at 350°C. Being another large-pore zeolite, bi-molecular hydride transfer reactions can occur during this reaction. As in ZSM-5 and zeolite Y, at high temperatures, olefins and aromatic products are released.

By Raman spectroscopy, with increasing temperature, we observe signal broadening in the C=C stretch region as in zeolite Y. From 50°C to 300°C, a shoulder at 1,530 cm⁻¹ develops that might be attributed to benzofuran formation, though this vibration is at a slightly lower vibrational frequency and its intensity is weaker than in ZSM-5. As in zeolite Y, there was a shoulder at 1,530 cm⁻¹ in the spectrum, acquired after adsorption at room temperature, and can likely be attributed to the formation of trimers. Again, at higher temperatures, the Raman spectrum seems to resemble a non-aromatic type coke. Data and discussion of the corresponding UV-vis experiment are given in Figure S8.

From the results above, we summarize that benzofuran formation dominates the chemistry on ZSM-5, driving the production of aromatics and small olefins. In contrast, ferrierite, which, under the applied conditions, restricts molecular transport to a single dimension (via 10-membered ring channels) and predominantly promotes direct hydrolysis of furan and its dimers, yielding propene and $\rm CO_2$ without aromatic formation. In the large-pore zeolites, Y and beta, the rapid formation of





conjugated hydrocarbons (long-chain alkenes or monocyclic species) is observed, with paraffins in the effluent indicating bimolecular hydride transfer. Such bi-molecular reactions are apparently hindered in medium-pore zeolites in this particular reaction and seem to require the large-pore zeolites. These findings highlight how ZSM-5 provides sufficient spatial constraint to prevent rapid hydrocarbon conjugation at intermediate temperatures but is less limited in its internal pore structure than the pore channel system of ferrierite to selectively form benzofuran.

Deciphering zeolite catalyst deactivation

Careful examination of the confined species present on the deactivated zeolites allows to shed further light on the intricate mechanism underlying catalyst deactivation. As seen in Figure 6A (i), by cooling the reactor after the reaction on ZSM-5 and recording a Raman spectrum at room temperature for a longer acquisition time (five times longer), we observe better-resolved signals that show more clearly the lowfrequency vibrations that identify polyaromatic hydrocarbons (630, 725, and 805 cm⁻¹)²¹ and planar CCC bonds typical of the trivalent C atoms in branched aromatics (587 cm⁻¹).²¹ In the C=C stretch region, two distinct bands can be observed, at 1,579 and 1,610 cm⁻¹, that correspond to C=C stretching vibrations in linear alkenes²¹ and naphthalenic or polyaromatic hydrocarbons, 19,34 respectively. A strong signal with two maxima, at 1,380 and 1,440 cm⁻¹, further confirms the presence of small polycyclic aromatic hydrocarbons, including naphthalene and fluorene. 19,34

In contrast, Raman spectra from other zeolites (Figure 6B) are more typical of carbon containing a strong sp³ character, having weaker bands in the 1,380 cm⁻¹ region with respect to that nearer to 1,600 cm⁻¹, which would correspond to amorphous carbon in regard to coke characterization; i.e., not graphitic in nature.⁴0 In ferrierite, one low-frequency vibration at 612 cm⁻¹ is an indicator of carbon branching as in planar C-C-C bonds.²¹ It is interesting to note that molecular polycyclic aromatic hydrocarbon species only form in ZSM-5 and not in large-pore zeolites despite enough internal volume to allow their formation.

Figure 4. Role of framework topology in catalytic intermediates: Ferrierite

(MS data were collected during the TPR of furan on ferrierite (A), and Kerr-gated Raman data were collected simultaneously in the same experiment (B). Spectra are shown from 100°C to 600°C at 100°C intervals. Measurements were performed at increasing reaction temperatures (i.e., heating up to 600°C at a rate of 5°C min⁻¹) under He gas flow after furan saturation at room temperature. Excitation was wavelength 400 nm.

These results align with the TGA data (Figure S9), which show clear differences in the type of coke formed on ZSM-5 compared to the other zeolite catalysts.

With respect to a pathway leading to the formation of polyaromatics in ZSM-5,

some research papers have discussed benzofuran as a coke precursor molecule to be avoided in order to enhance catalyst lifetime ⁴¹ or as a coke molecule itself in low-temperature reactions. ³⁸ In our Raman data, the formation of polyaromatics is seen at 500°C and above, whereas the consumption of benzofuran is observed below 400°C, ruling out a pathway wherein benzofuran is directly responsible for forming polyaromatic hydrocarbons. Furthermore, the coincidence of the formation of monocyclic aromatic hydrocarbons as recorded by MS with the consumption of benzofuran as detected by Raman spectroscopy suggests that benzofuran further reacts to form monocyclic aromatic hydrocarbons. This evidence renders benzofuran an active species as opposed to one responsible for deactivation.

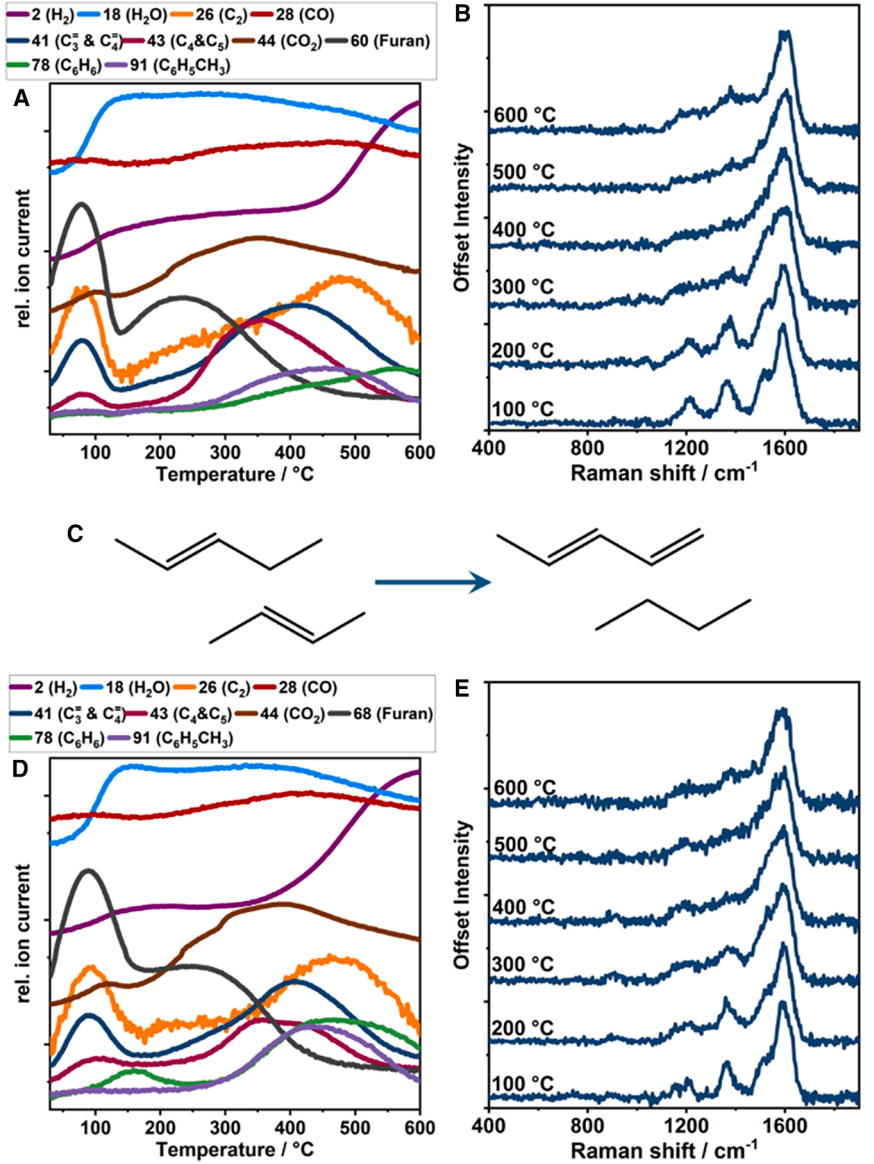
These results provide direct and comprehensive evidence of how the zeolite topology leads to different product selectivities and deactivation pathways. The scheme given in Figure 6C summarizes the general pathway to the mechanism observed in ZSM-5, where benzofuran is detected by spectroscopy as an intermediate, then aromatic products are detected by MS from the outlet of the reactor, and polyaromatic hydrocarbons are later detected by spectroscopy as inactive coke species, possibly through consecutive aromatic condensation reactions. We do not rule out a role of small olefins (C_2-C_4) in the reaction but are unable to observe these by Raman spectroscopy using a 400 nm excitation source; rather, it would require the use of a UV Raman excitation source, which cannot be used with a Kerrmedium to block fluorescence, in this case causing Raman signals to be obscured, as shown in Figure S4.⁴²

HCP mechanism in CFP?

HCP chemistry has been previously discussed in the context of CFP owing to the formation of a complex mixture of adsorbed furans, aromatics (arising from benzofuran intermediates, as shown above), and olefinic species. Olefins are generated either through furan decarbonylation to propadiene, followed by oligomerization and cracking, or via furan hydrolysis, which yields olefins and ${\rm CO_2}^{.38}$ This mixture closely resembles the HCP generated during the MTH reaction, so an analogous mechanism has been proposed. 31,43

Article





In further inspection of the spectrum acquired at the end of the reaction on ZSM-5, previous experiments for the MTH reaction on ZSM-5 show, remarkably, that similar species have formed after the reaction, as exhibited in Figure 6A (ii). Both spectra show evidence of aliphatic and aromatic C=C stretching at 1,580 and 1,610 cm⁻¹,^{19,21} ring-breathing vibrations of bi- or polycyclic aromatic hydrocarbons at 1,360–1,386 cm⁻¹, and a shoulder at 1,445 cm⁻¹, where we identify bent polyaromatic structures such as fluorene or phenanthrene. ^{19,34} A greater number of low-frequency vibrations after the reaction of furan show more severe formation of polyaromatic hydrocarbons. ²¹ This is in line with the use of

furan having a lower C/H_{eff} than methanol, leading to a higher

degree of coke formation, - also influenced by the higher reac-

tion temperature (600°C) for furan conversion as opposed to

that of the MTH reaction (450°C).

Figure 5. Role of framework topology in catalytic intermediates: Zeolite Y and beta (A and B) MS data collected during the TPR of furan on zeolite Y (A), and Kerr-gated Raman data were collected simultaneously in the same experiment. Spectra are shown from 100°C to

600°C at 100°C intervals.

(C) Scheme depicting the chemical pathway in bimolecular hydride transfer between two alkenes to form a paraffin and a more conjugated alkene. (D and E) MS data collected during TPR of furan on zeolite beta (D), and Kerr-gated Raman data were collected simultaneously in the same experiment, showing spectra from 100°C to 600°C at 100°C intervals.

Measurements were performed at increasing reaction temperatures (up to 600°C at a rate of 5°C min⁻¹) under He gas flow after furan saturation at room temperature. Excitation wavelength was 400 nm

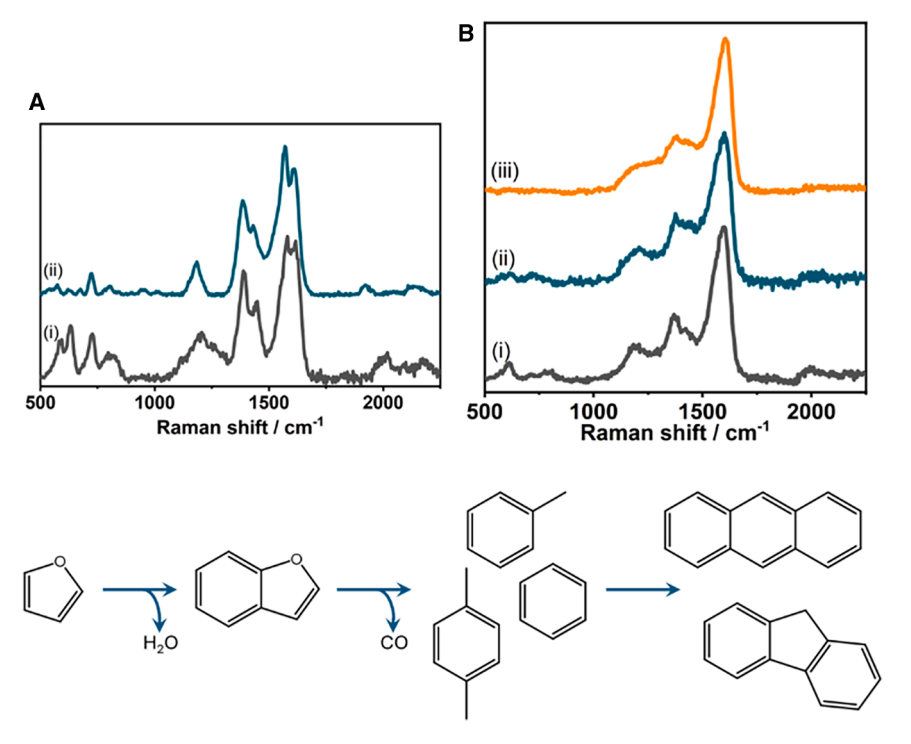
Nonetheless, the similarities in the adsorbed species formed after reaction suggest that CFP and MTH reaction mechanisms might have much in common, further supporting the idea that the reaction of furan over ZSM-5 proceeds through an HCP mechanism involving the initial formation of benzofuran via Diels-Alder condensation. The benzofuran intermediate subsequently plays a key role in generating aromatics and small olefins that constitute the HCP, sustaining the catalytic cycle.

In summary, the application of operando Kerr-gated Raman spectroscopy, in combination with computational simulations, provides direct evidence that the chemical pathways and adsorbed intermediates in CFP are defined by the zeolite framework topology. In ZSM-5, we observe a clear temporal correlation

showing that benzofuran forms early in the reaction, coinciding with the onset of aromatic production, and decays well before the onset of coke formation. This rules out its role as a coke precursor, a long-standing assumption, and identifies it instead as a key intermediate in the selective formation of aromatics and small olefins.

Topological effects are further evidenced by contrasting behavior across different zeolite frameworks. Ferrierite, which acts as a 1-dimensional system due to steric constraints, predominantly promotes direct hydrolysis of furan and its dimers, yielding propene and carbon dioxide without aromatic formation, whereas the large-pore zeolites Y and beta favor the formation of conjugated hydrocarbons through bi-molecular reactions—hindered in medium-pore zeolites. These results contrast sharply with those observed for ZSM-5 and provide strong evidence of topological effects, particularly the role of





MFI channel intersections in the formation of benzofuran intermediates crucial to aromatic production.

These findings clearly evidence how ZSM-5 zeolite provides an optimal balance: sufficient spatial confinement to limit bi-molecular reaction while enabling pathways leading to benzofuran formation and subsequent aromatic production. Furthermore, the observation of similar spectroscopic signatures between MTH and CFP reactions provide further evidence of the involvement of a HCP mechanism initiated through benzofuran and the subsequent formation of both aromatics and small olefins, likely establishing the HCP.

Overall, this work reveals a previously unestablished relationship between zeolite topology and intermediate reactivity in CFP. By clarifying the role of benzofuran as a non-deactivating intermediate and showing how its formation and fate depend on framework geometry, we provide insight into how catalyst structure directs selectivity and lifetime. These findings offer a platform for more targeted catalyst design strategies in biomass conversion, based on structure-function correlations rather than empirical screening.

METHODS

Materials and characterization

ZSM-5 was synthesized using a nominal Si/Al ratio of 15. Sodium aluminate (0.0910 g, Sigma-Aldrich) was added to deionized water (4.8 g). Tetraethyl orthosilicate (5.847 g, >99.8%, Sigma-Aldrich) was added dropwise to the solution, followed by tetrapropylammonium hydroxide (2.8935 g, 40% solution in water) with additional deionized water (2.8 g). The gel was stirred for 45 min before it was transferred to a Teflon-lined autoclave. The synthesis was carried out at 180°C for 22 h. After the crystal-

Figure 6. Carbon fingerprints in deactivated catalysts

(A and B) Kerr-gated Raman spectra collected at the end of TPR of furan on (A) H-ZSM-5 (i) and MTH on H-ZSM-5 (ii) and (B) ferrierite (i), zeolite beta (ii), and zeolite Y (iii).

(C) Chemical pathways observed in ZSM-5 after TPR of furan.

lization, the autoclave was guenched. The solid was filtered, washed with 5 dm3 of deionized water until neutral pH, and dried overnight at 70°C. The zeolite was calcined in static air to remove the organic template at 550°C for 8 h, ion-exchanged with a 1 M solution of NH₄NO₃ at 80°C for 10 h, and washed with 3 dm³ of deionized water. This was repeated a further two times to yield NH₄-ZSM-5. The zeolite was calcined at 550°C for 4 h to obtain the proton form zeolite. Ferrierite (CP914C), and beta (CP814E) were purchased from Zeolyst International in their ammonium forms and calcined by muffle furnace at 550°C

for 4 h to yield their proton forms prior to reaction or characterization. Zeolite Y (CBV720) was purchased in proton form from Zeolyst International.

The as-synthesized ZSM-5 was characterized by powder X-ray diffraction (PXRD) to confirm phase and purity. The powder diffraction pattern was collected on a Rikagu SmartLab with a 9 kW Cu source. Measurements were recorded over the range of 20 from 5° to 55°. During measurement, the sample spins at 1 °min $^{-1}$ to avoid any preferred orientation of the powder. The as-synthesized ZSM-5 was also characterized by X-ray fluorescence (XRF) to confirm the expected Si/Al ratio. All zeolites were further studied by $\rm N_2$ physisorption and $\rm NH_3$ -TPD. $\rm N_2$ physisorption was carried out on a Quadrasorb Brunauer-Emmett-Teller (BET) after degassing each sample under a vacuum at 350°C for 20 h to remove any adsorbed species. Surface areas were analyzed using the BET plot using 5 points between 0.001 and 0.011 relative pressure. Micropore volume was analyzed using the t-plot method, selecting 6 points between 0.3 and 0.5 relative pressure.

Operando Kerr-gated Raman spectroscopy

Kerr-gated Raman requires two pulsed laser beams. A Ti-sapphire laser emitting an 800 nm fundamental wavelength at a 10 kHz repetition rate was used, with its pulse width tuned to 2 ps. To activate the Kerr gate, 0.24 mJ of the fundamental 800 nm beam (the gating beam) is focused by a lens to a spot of 1 mm diameter on the Kerr cell. The polarization of the gating beam is at 45° between the two orthogonal polarizers in the Kerr gate. CS_2 was used as a Kerr medium. 350 mW of the 800 nm fundamental beam is split to generate 120 mW of the second harmonic at 400 nm to be used as a Raman probe, which is set to a parallel polarization at the sample. The beam is focused by a lens to a spot size of 100 μm on the sample, initiating its

Article



Raman scattering. The Raman signal must arrive at the Kerr cell at the same time as the gating pulse, this is controlled by sending the 400 nm probe beam via a delay line-a motorized linear stage containing a hollow retroreflector. The delay line allows the arrival time of the excitation pulse at the sample to be adjusted and optimized to give the strongest Raman signal. Throughout the experiment, several time delays are recorded around the optimal time to ensure that, during the experiment, the best Raman signal is recorded. The signal that passes through the Kerr gate is dispersed and detected by a Czerny-Turner spectrograph (Shamrock 303i, Andor) equipped with a charge-coupled device (CCD) camera (iDus DU-420A-BU2, Andor), which is calibrated by recording the Raman spectrum of toluene. The grating used in the system is 1,200 lines/mm. The CCD contains a silicone sensor of 1,024 × 2,56 pixels. To block the Rayleigh scattering, a RazorEdge LP02-407RU edge filter was used between the sample and the Kerr gate; the tilt of the filter was carefully adjusted to match the spectral position of the cutoff edge with the probe wavelength.

Since the samples were highly absorbing at 400 nm, to avoid laser damage to the sample, a low power (1 mW) was employed for the Raman measurements, and measurements were taken for 2 \times 4 s acquisitions. The Linkam cell was fitted to a stage that rapidly moves horizontally on both x and y axes by approximately 2-3 mm, which further helps to mitigate sample damage by moving the sample in the beam to avoid focusing on one spot that might induce photodamage or thermal heating of the sample. During these experiments, 50 mg of zeolite catalyst was pre-treated by heating at 10°C min⁻¹ in a flow of 20% O₂/He to 600°C and holding for 1 h in the Linkam CCR1000 cell. The catalyst was then cooled to 30°C in He, and then furan was adsorbed by injection by a syringe pump at 6 μL/min for 1 h into the He stream, followed by flushing with He for 1 h to remove much of the weakly adsorbed species. The temperature was linearly increased by 5°C/min from 30°C to 600°C, and Raman spectra were recorded every 25°C; i.e., every 5 min. A Pfeiffer Omnistar GSD 320 mass spectrometer was used as an on-line gas analyzer to detect products out of the catalyst bed. MS was fitted with a tungsten filament using a secondary electron multiplier and 1 s sampling time.

UV-vis spectroscopy

For UV-vis experiments, the same catalyst treatment and conditions as used for the Kerr-gated Raman measurements were applied, and the CCR1000 stage was used again. The UV-vis experiments were carried out using a modular spectrometer from Ocean Optics, comprising a Flame-S-XR1-ES Ocean Optics spectrometer with 100 μm slit, DH-2000-S-SUV-TTL light source, and QR400-7-SR-BX reflection probe (fiberoptic probe). The probe was held to the quartz window using the probe holder at a 45° angle to the sample; therefore, the diffusely reflected light was collected back at that same angle. UV-vis spectra were recorded over a total of 20 s in reflectance mode, using the calcined zeolite as a background, and the R% was converted to absorbance using the Kubelka-Munk formula.

Computational methods

Gas phase properties were calculated using the DMol³ module within the Materials Studio program. 44,45 The calculations were

performed at the RPBE/DNP level. ⁴⁶ A fine integration grid was used alongside the concurrent level of self-consistent field (SCF) convergence criteria. Charges were calculated via Mulliken analysis. ⁴⁷ Orbitals were generated at an isovalue of 0.03. Electronic excitations were calculated via time-dependent density functional theory (TDDFT).

Periodic properties were calculated using the QMERA module within the Materials Studio program. AB QMERA is a layered method that utilizes DMol for the atoms treated at the quantum mechanical (QM) level and GULP for those calculated at the molecular mechanical (MM) level. The atoms in the bound molecule (as per the gas phase calculations) were treated at the QM level. The framework was treated at the MM level with a smeared charge in order to balance the system where appropriate. The QM level was run at the RPBE/DNP level of theory with a fine integration grid and subsequently tightened SCF convergence criteria. Charges were calculated in the QM region via Mulliken analysis. Torbitals were generated at an isovalue of 0.03. Electronic excitations were calculated via TDDFT. Due to the periodic nature of the calculations, subtractive mechanical embedding was used.

A comparison of the methods for generating Raman spectra is given in Tables S3 and S4 and Figure S10.

TGA of spent catalyst samples

TGA was performed on a Q50 thermogravimetric analyzer from TA instruments. Around 10 mg of the used catalyst was loaded into a platinum pan, which was loaded into the furnace of the instrument. The sample was heated at a rate of 5°C min⁻¹ to 900°C under a flow of 60 mL min⁻¹ air. The mass of the sample is weighed and recorded throughout the temperature ramp to detect changes.

RESOURCE AVAILABILITY

Lead contact

Requests for further information and resources should be directed to and will be fulfilled by the lead contact, Andrew M. Beale (andrew.beale@ucl.ac.uk).

Materials availability

This study did not generate new unique materials.

Data and code availability

- All data reported in this paper will be shared by the lead contact upon request
- This paper does not report original code.
- Any additional information required to reanalyze the data reported in this
 paper is available from the lead contact upon request.

ACKNOWLEDGMENTS

The authors acknowledge EPSRC (EP/R026939/1, EP/R026815/1, and EP/S016147/1) for funding. The ISIS characterization laboratory is also gratefully acknowledged for the collection of XRD data.

AUTHOR CONTRIBUTIONS

Conceptualization, M.J.W., M.T., A.M.B., and I.L.-G.; methodology, E.C., I.V.S., and I.L.-G.; investigation, E.C., I. V.S., J.M., P.C., M.P., S.K., and I.L.-G.; formal analysis, E.C., and J.M.; validation, E.C., and J.M.; visualization, E.C.; writing – original draft, E.C.; writing – review & editing, all authors; funding



Cell Reports Physical Science Article

acquisition, I.L.-G., M.J.W., M.T., and A.M.B.; supervision, I.L.-G., I.V.S., C.S.B., P.C., and A.M.B.

DECLARATION OF INTERESTS

A.M.B. is a director and shareholder in Finden Ltd. and Methanox Ltd.

SUPPLEMENTAL INFORMATION

Supplemental information can be found online at https://doi.org/10.1016/j.xcrp.2025.102858.

Received: April 16, 2025 Revised: July 30, 2025 Accepted: August 29, 2025 Published: September 23, 2025

REFERENCES

- Liu, C., Wang, H., Karim, A.M., Sun, J., and Wang, Y. (2014). Catalytic fast pyrolysis of lignocellulosic biomass. Chem. Soc. Rev. 43, 7594–7623. https://doi.org/10.1039/C3CS60414D.
- Carlson, T.R., Cheng, Y.-T., Jae, J., and Huber, G.W. (2011). Production of green aromatics and olefins by catalytic fast pyrolysis of wood sawdust. Energy Environ. Sci. 4, 145–161. https://doi.org/10.1039/C0EE00341G.
- Runnebaum, R.C., Nimmanwudipong, T., Doan, J., Block, D.E., and Gates, B.C. (2012). Catalytic Conversion of Furan to Gasoline-Range Aliphatic Hydrocarbons via Ring Opening and Decarbonylation Reactions Catalyzed by Pt/γ-Al2O3. Catal. Lett. 142, 664–666. https://doi.org/10. 1007/s10562-012-0816-2.
- Jae, J., Tompsett, G.A., Foster, A.J., Hammond, K.D., Auerbach, S.M., Lobo, R.F., and Huber, G.W. (2011). Investigation into the shape selectivity of zeolite catalysts for biomass conversion. J. Catal. 279, 257–268. https:// doi.org/10.1016/j.jcat.2011.01.019.
- Carlson, T.R., Vispute, T.P., and Huber, G.W. (2008). Green Gasoline by Catalytic Fast Pyrolysis of Solid Biomass Derived Compounds. ChemSusChem 1, 397–400. https://doi.org/10.1002/cssc.200800018.
- Hernando, H., Hernández-Giménez, A.M., Ochoa-Hernández, C., Bruijnincx, P.C.A., Houben, K., Baldus, M., Pizarro, P., Coronado, J.M., Fermoso, J., Čejka, J., et al. (2018). Engineering the acidity and accessibility of the zeolite ZSM-5 for efficient bio-oil upgrading in catalytic pyrolysis of lignocellulose. Green Chem. 20, 3499–3511. https://doi.org/10.1039/c8gc01722k.
- Uslamin, E.A., Luna-Murillo, B., Kosinov, N., Bruijnincx, P.C.A., Pidko, E.A., Weckhuysen, B.M., and Hensen, E.J.M. (2019). Gallium-promoted HZSM-5 zeolites as efficient catalysts for the aromatization of biomassderived furans. Chem. Eng. Sci. 198, 305–316. https://doi.org/10.1016/j. ces.2018.09.023.
- Zheng, Y., Wang, F., Yang, X., Huang, Y., Liu, C., Zheng, Z., and Gu, J. (2017). Study on aromatics production via the catalytic pyrolysis vapor upgrading of biomass using metal-loaded modified H-ZSM-5. J. Anal. Appl. Pyrolysis 126, 169–179. https://doi.org/10.1016/j.jaap.2017.06.011.
- Uslamin, E.A., Kosinov, N., Filonenko, G.A., Mezari, B., Pidko, E., and Hensen, E.J.M. (2019). Co-Aromatization of Furan and Methanol over ZSM-5—A Pathway to Bio-Aromatics. ACS Catal. 9, 8547–8554. https:// doi.org/10.1021/acscatal.9b02259.
- Qi, X., and Fan, W. (2019). Selective Production of Aromatics by Catalytic Fast Pyrolysis of Furan with In Situ Dehydrogenation of Propane. ACS Catal. 9, 2626–2632. https://doi.org/10.1021/acscatal.8b04859.
- Yarulina, I., Chowdhury, A.D., Meirer, F., Weckhuysen, B.M., and Gascon, J. (2018). Recent trends and fundamental insights in the methanol-to-hydrocarbons process. Nat. Catal. 1, 398–411. https://doi.org/ 10.1038/s41929-018-0078-5.
- Olsbye, U., Svelle, S., Lillerud, K.P., Wei, Z.H., Chen, Y.Y., Li, J.F., Wang, J.G., and Fan, W.B. (2015). The formation and degradation of active

- species during methanol conversion over protonated zeotype catalysts. Chem. Soc. Rev. 44, 7155–7176. https://doi.org/10.1039/C5CS00304K.
- Carlson, T.R., Jae, J., and Huber, G.W. (2009). Mechanistic Insights from Isotopic Studies of Glucose Conversion to Aromatics Over ZSM-5. ChemCatChem 1, 107–110. https://doi.org/10.1002/cctc.200900130.
- Mukarakate, C., Watson, M.J., ten Dam, J., Baucherel, X., Budhi, S., Yung, M.M., Ben, H., Iisa, K., Baldwin, R.M., and Nimlos, M.R. (2014). Upgrading biomass pyrolysis vapors over β-zeolites: role of silica-to-alumina ratio. Green Chem. 16, 4891–4905. https://doi.org/10.1039/C4GC01425A.
- Luna Murillo, B. (2020). Aromatization of Oxygenates over Zeolite Catalysts. https://doi.org/10.33540/191.
- Uslamin, E.A., Kosinov, N.A., Pidko, E.A., and Hensen, E.J.M. (2018).
 Catalytic conversion of furanic compounds over Ga-modified ZSM-5 zeolites as a route to biomass-derived aromatics. Green Chem. 20, 3818–3827. https://doi.org/10.1039/C8GC01528G.
- 17. Pan, Z., Wu, X., Bodi, A., van Bokhoven, J.A., and Hemberger, P. (2024). Catalytic pyrolysis mechanism of lignin moieties driven by aldehyde, hydroxyl, methoxy, and allyl functionalization: the role of reactive quinone methide and ketene intermediates. Green Chem. 26, 9899–9910.
- Hemberger, P., Custodis, V.B.F., Bodi, A., Gerber, T., and van Bokhoven, J.A. (2017). Understanding the mechanism of catalytic fast pyrolysis by unveiling reactive intermediates in heterogeneous catalysis. Nat. Commun. 8, 15946. https://doi.org/10.1038/ncomms15946.
- Allotta, P.M., and Stair, P.C. (2012). Time-Resolved Studies of Ethylene and Propylene Reactions in Zeolite H-MFI by In-Situ Fast IR Heating and UV Raman Spectroscopy. ACS Catal. 2, 2424–2432. https://doi.org/10. 1021/cs3004215.
- Matousek, P., Towrie, M., Stanley, A., and Parker, A.W. (1999). Efficient Rejection of Fluorescence from Raman Spectra Using Picosecond Kerr Gating. Appl. Spectrosc. 53, 1485–1489.
- Lezcano-Gonzalez, I., Campbell, E., Hoffman, A.E.J., Bocus, M., Sazanovich, I.V., Towrie, M., Agote-Aran, M., Gibson, E.K., Greenaway, A., De Wispelaere, K., et al. (2020). Insight into the effects of confined hydrocarbon species on the lifetime of methanol conversion catalysts. Nat. Mater. 19, 1081–1087. https://doi.org/10.1038/s41563-020-0800-y.
- Osatiashtiani, A., Zhang, J., Stefanidis, S.D., Zhang, X., and Bridgwater, A.V. (2022). The mechanism for catalytic fast pyrolysis of levoglucosan, furfural and furan over HZSM-5: An experimental and theoretical investigation. Fuel 328, 125279. https://doi.org/10.1016/j.fuel.2022.125279.
- Cheng, Y.-T., and Huber, G.W. (2011). Chemistry of Furan Conversion into Aromatics and Olefins over HZSM-5: A Model Biomass Conversion Reaction. ACS Catal. 1, 611–628. https://doi.org/10.1021/cs200103j.
- Cheng, Y.-T., and Huber, G.W. (2012). Production of targeted aromatics by using Diels-Alder classes of reactions with furans and olefins over ZSM-5. Green Chem. 14, 3114–3125. https://doi.org/10.1039/C2GC35767D.
- Spoto, G., Geobaldo, F., Bordiga, S., Lamberti, C., Scarano, D., and Zecchina, A. (1999). Heterocycles oligomerization in acidic zeolites: a UV-visible and IR study. Top. Catal. 8, 279–292. https://doi.org/10.1023/ A:1019137900710.
- Psarras, A.C., Michailof, C.M., Iliopoulou, E.F., Kalogiannis, K.G., Lappas, A.A., Heracleous, E., and Triantafyllidis, K.S. (2019). Acetic acid conversion reactions on basic and acidic catalysts under biomass fast pyrolysis conditions. Mol. Catal. 465, 33–42. https://doi.org/10.1016/j.mcat.2018.
- Ji, Y., Pan, J., Dauenhauer, P., and Gorte, R.J. (2019). Probing direct carbon-carbon acylation of furans and long-chain acids over H-ZSM-5. Appl. Catal. Gen. 577, 107–112. https://doi.org/10.1016/j.apcata.2019.03.012.
- Gumidyala, A., Sooknoi, T., and Crossley, S. (2016). Selective ketonization of acetic acid over HZSM-5: The importance of acyl species and the influence of water. J. Catal. 340, 76–84. https://doi.org/10.1016/j.jcat.2016.04.017.
- Singh, V.B. (2006). Ab initio and DFT studies of the vibrational spectra of benzofuran and some of its derivatives. Spectrochim. Acta Mol. Biomol. Spectrosc. 65, 1125–1130. https://doi.org/10.1016/j.saa.2006.01.045.

Article



- Vaitheeswaran, S., Green, S.K., Dauenhauer, P., and Auerbach, S.M. (2013). On the Way to Biofuels from Furan: Discriminating Diels–Alder and Ring-Opening Mechanisms. ACS Catal. 3, 2012–2019. https://doi. org/10.1021/cs4003904.
- Liu, C., Evans, T.J., Cheng, L., Nimlos, M.R., Mukarakate, C., Robichaud, D.J., Assary, R.S., and Curtiss, L.A. (2015). Catalytic Upgrading of Biomass-Derived Compounds via C-C Coupling Reactions: Computational and Experimental Studies of Acetaldehyde and Furan Reactions in HZSM-5. J. Phys. Chem. C 119, 24025–24035. https://doi.org/10.1021/ acs.jpcc.5b08141.
- Shao, S., Zhang, H., Xiao, R., Shen, D., and Zheng, J. (2013). Comparison of Catalytic Characteristics of Biomass Derivates with Different Structures Over ZSM-5. Bioenerg. Res. 6, 1173–1182. https://doi.org/10.1007/s12155-013-9303-x.
- Socrates, J. (2001). Infrared and Raman Characteristic Group Frequencies Tables and Charts 3rd ed. (John Wiley and Sons).
- Signorile, M., Bonino, F., Damin, A., and Bordiga, S. (2015). In Situ Resonant UV-Raman Spectroscopy of Polycyclic Aromatic Hydrocarbons. J. Phys. Chem. C 119, 11694–11698. https://doi.org/10. 1021/acs.jpcc.5b02209.
- Borodina, E., Meirer, F., Lezcano-González, I., Mokhtar, M., Asiri, A.M., Al-Thabaiti, S.A., Basahel, S.N., Ruiz-Martinez, J., and Weckhuysen, B.M. (2015). Influence of the Reaction Temperature on the Nature of the Active and Deactivating Species during Methanol to Olefins Conversion over H-SSZ-13. ACS Catal. 5, 992–1003. https://doi.org/10.1021/ cs501345q.
- Blitz, J.P. (1998). Diffuse Reflectance Spectroscopy. In Modern Techniques in Applied Molecular Spectroscopy (John Wiley & Sons), pp. 185–220.
- Milosevic, M., and Berets, S.L. (2002). A Review of Ft-Ir Diffuse Reflection Sampling Considerations. Appl. Spectrosc. Rev. 37, 347–364. https://doi. org/10.1081/ASR-120016081.
- Gilbert, C.J., Espindola, J.S., Conner, W.C., Trierweiler, J.O., and Huber, G.W. (2014). The Effect of Water on Furan Conversion over ZSM-5. Chem-CatChem 6, 2497–2500. https://doi.org/10.1002/cctc.201402390.
- Haw, J.F., Song, W., Marcus, D.M., and Nicholas, J.B. (2003). The Mechanism of Methanol to Hydrocarbon Catalysis. Acc. Chem. Res. 36, 317–326. https://doi.org/10.1021/ar020006o.
- Sattler, J.J.H.B., Beale, A.M., and Weckhuysen, B.M. (2013). Operando Raman spectroscopy study on the deactivation of Pt/Al2O3 and Pt-Sn/ Al2O3 propane dehydrogenation catalysts. Phys. Chem. Chem. Phys. 15, 12095–12103. https://doi.org/10.1039/c3cp50646k.

- Gancedo, J., Faba, L., and Ordóñez, S. (2021). Benzofuran as deactivation precursor molecule: Improving the stability of acid zeolites in biomass pyrolysis by co-feeding propylene. Appl. Catal. Gen. 611, 117980. https://doi.org/10.1016/j.apcata.2020.117980.
- Campbell, E., Sazanovich, I.V., Towrie, M., Watson, M.J., Lezcano-Gonzalez, I., and Beale, A.M. (2024). Methanol-to-Olefins Studied by UV Raman Spectroscopy as Compared to Visible Wavelength: Capitalization on Resonance Enhancement. J. Phys. Chem. Lett. 15, 6826–6834. https://doi.org/10.1021/acs.jpclett.4c00865.
- Liang, J., Shan, G., and Sun, Y. (2021). Catalytic fast pyrolysis of lignocellulosic biomass: Critical role of zeolite catalysts. Renew. Sustain. Energy Rev. 139, 110707. https://doi.org/10.1016/j.rser.2021.110707.
- Delley, B. (1990). An all-electron numerical method for solving the local density functional for polyatomic molecules. J. Chem. Phys. 92, 508–517. https://doi.org/10.1063/1.458452.
- Delley, B. (2000). From molecules to solids with the DMol3 approach.
 J. Chem. Phys. 113, 7756–7764. https://doi.org/10.1063/1.1316015.
- Hammer, B., Hansen, L.B., and Nørskov, J.K. (1999). Improved adsorption energetics within density-functional theory using revised Perdew-Burke-Ernzerhof functionals. Phys. Rev. B 59, 7413–7421. https://doi.org/10. 1103/PhysRevB.59.7413.
- Mulliken, R.S. (1955). Electronic Population Analysis on LCAO–MO Molecular Wave Functions. I. J. Chem. Phys. 23, 1833–1840. https://doi.org/10. 1063/1.1740588
- Sherwood, P., de Vries, A.H., Guest, M.F., Schreckenbach, G., Catlow, C.R.A., French, S.A., Sokol, A.A., Bromley, S.T., Thiel, W., Turner, A.J., et al. (2003). QUASI: A general purpose implementation of the QM/MM approach and its application to problems in catalysis. J. Mol. Struct.: THEOCHEM 632, 1–28. https://doi.org/10.1016/S0166-1280 (03)00285-9.
- Eichler, U., Kölmel, C.M., and Sauer, J. (1997). Combining ab initio techniques with analytical potential functions for structure predictions of large systems: Method and application to crystalline silica polymorphs. J. Comput. Chem. 18, 463–477. https://doi.org/10.1002/(SICI)1096-987X (199703)18:4<463::AID-JCC2>3.0.CO;2-R.
- Sierka, M., and Sauer, J. (1997). Structure and reactivity of silica and zeolite catalysts by a combined quantum mechanics[ndash]shell-model potential approach based on DFT. Faraday Discuss 106, 41–62. https:// doi.org/10.1039/A701492I.
- Sierka, M., and Sauer, J. (2000). Finding transition structures in extended systems: A strategy based on a combined quantum mechanics—empirical valence bond approach. J. Chem. Phys. 112, 6983–6996. https://doi.org/ 10.1063/1.481296.